



Science Arts & Métiers (SAM)

is an open access repository that collects the work of Arts et Métiers Institute of Technology researchers and makes it freely available over the web where possible.

This is an author-deposited version published in: <https://sam.ensam.eu>
Handle ID: <http://hdl.handle.net/10985/21766>

To cite this version :

Khaoula RAHMOUNI, Aurélien BESNARD, Kafia OULMI, Corinne NOUVEAU, Aissam HIDOUSI, Linda AISSANI, Mourad ZAABAT - In vitro corrosion response of CoCrMo and Ti-6Al-4V orthopedic implants with Zr columnar thin films - Surface and Coatings Technology - Vol. 436, p.128310 - 2022

Any correspondence concerning this service should be sent to the repository

Administrator : scienceouverte@ensam.eu



In vitro corrosion response of CoCrMo and Ti-6Al-4V orthopedic implants with Zr columnar thin films

Khaoula Rahmouni^{a,b}, Aurélien Besnard^{a,*}, Kafia Oulmi^c, Corinne Nouveau^a, Aissam Hidoussi^d, Linda Aissani^b, Mourad Zaabat^b

^a Arts et Metiers Institute of Technology, LaBoMaP, Université Bourgogne Franche-Comté, HESAM Université, Rue Porte de Paris, F-71250 Cluny, France

^b Active Components and Materials Laboratory, Larbi BEN M'HIDI University, Oum El Bouaghi 04000, Algeria

^c Laboratory of Electrochemistry, Faculty of Material Sciences, Batna University 1, Batna 05000, Algeria

^d Laboratory of Physico-Chemical Study of Materials, Faculty of Material Sciences, Batna University 1, Batna 05000, Algeria

ARTICLE INFO

Keywords:

Oblique angle deposition (OAD)

DC magnetron sputtering

Zr films

CoCrMo and Ti-6Al-4V alloys

Corrosion resistance

Porosity

ABSTRACT

This study focuses on the functionalized modification of Ti-6Al-4V and CoCrMo alloys substrates widely used by the biomedical domain as total joint replacements (TJR) of the hip and knee. To improve the corrosion resistance of these devices, nanostructured columnar zirconium (Zr) thin films were produced by oblique angle deposition (OAD) using DC magnetron sputtering to model the particular design of the joint. The influence of the angular distribution of the incoming particle flux on the resulting film morphology (column tilt angle, porosity) and electrochemical behavior was studied by varying the substrates inclination angle θ from 15 to 90°. The experimental deposition process was reproduced by kinetic Monte Carlo (kMC) models. With the increase of the flux incidence angle α from 0 to 70°, the film thickness and the column tilt angle β vary in agreement with the theoretical models. Additionally, the corrosion behavior of uncoated and Zr-coated alloys (CoCrMo and Ti-6Al-4V) was compared through open circuit potential chronopotentiometry and electrochemical polarization test in NaCl 0.9% solution at 37 °C. It was found that the corrosion protection was successfully improved by the presence of the films. The variation of the corrosion behavior with the flux incidence angle is explained by the changes in the film density.

1. Introduction

Total joint replacements (TJR) of hip and knee, designed to retain mobility and reduce pain, have been widely used in surgical operations [1,2]. The number of hip and knee replacements increased by 15–22% worldwide in the last decade [3]. Kurtz et al. [4] predicted that the primary hip and knee arthroplasty would grow by 174% and 673%, respectively, in the United States between 2005 and 2030. Besides, more and more younger people are requiring hip or knee joint replacement, thus generating demand for longer service life for these artificial devices [5]. Current total hip and knee replacements using modern designs and materials, appropriate patient selection, and surgical techniques have satisfactory results that last 15 years longer for most patients [6]. However, the detachment of wear particles remains one of the main problems, e.g. wear debris, especially UHMWPE (Ultra-high-molecular-weight polyethylene) particles from Metal-on-Polymer (MoP) joints, may cause aseptic loosening [7]. In order to overcome this problem,

alternative bearings such as Metal-on-Metal (MoM) prostheses, including CoCrMo and Ti-6Al-4V components, have been developed. The second generation of MoM bearings was introduced in the early 90s [8]. Among metallic biomaterials, titanium (Ti) and its alloys are given preference to use as orthopedic implants. Indeed, Ti alloys display good mechanical strength, good resistance to corrosion process in an aggressive medium, low density (4.43 g.cm⁻³), as well as good biocompatibility [9–12]. However, the Ti-6Al-4V exhibits also low hardness, relatively low Young's modulus (101–120 MPa), and poor resistance to combined wear and corrosion processes [13,14]. When the Ti-6Al-4V is exposed to aggressive media, the passive oxide film spontaneously formed on the surface is broken [15]. Moreover, this protection is not enough to ensure the proper performance of this material when implanted in the human body. Biomedical CoCrMo alloys are also widely used in implants owing to their excellent mechanical properties, good biocompatibility, and high corrosion resistance [16–18]. Therefore, even if those alloys are among the most wear- and corrosion-

* Corresponding author.

E-mail address: aurelien.besnard@ensam.eu (A. Besnard).

resistant used, there is a need for a better control of the implants. Effective protection from the corrosion media can be accomplished by adding a coating on the base materials of the joint [9,19–23]. However, to provide adequate protection, the coating must be uniform, adhesive, pore-free, corrosion-resistant, and biocompatible [24,25]. Zirconium is one of the best candidates: it has excellent erosion resistance, biocompatibility, high hardness, good lubricity, and ductility properties [26–33]. In addition, due to the particular design of the joint, and its hemispherical shape with axial symmetry, the range and incidence angle effects on the protection should be studied. This study aims to evaluate the corrosion resistance of Zr coatings fabricated on total hip and knee prostheses made of Ti-6Al-4V and CoCrMo. The oblique angle deposition technique is used to model the deposition on a hemispherical shape by DC magnetron sputtering and design a dedicated substrate holder with substrate angles in the 15–90° range with 15° increments. Process simulation allows determining the flux incidence angles, responsible for the change of the inclined columnar microstructure of the films and the subsequent change in the properties of the films. The resulting Zr film's surface morphology, thickness, and electrochemical behavior were determined as a function of flux incidence angle.

2. Experimental details

2.1. Deposition conditions

Zr films were synthesized by a DC magnetron sputtering system using a circular (50.8 mm in diameter, 6 mm thick) zirconium metallic target (purity 99.99%). Substrate materials were Si (100) square pieces (10 mm sides' length and 0.38 mm in thickness), Ti-6Al-4V ELI (Grade 23) discs (12 mm in diameter, 3 mm in thickness), and CoCrMo discs (8.9 mm in diameter, 3 mm in thickness). The Ti-6Al-4V and CoCrMo metallic substrates were polished by SiC papers (from 180 down to 1200 grit) and finished with a 9- μ m diamond suspension in order to obtain a roughness of 30 to 38 nm (Ra). All substrates underwent ultrasonic cleaning in acetone for 15 min, then were rinsed in ethanol and dried. Afterward, they were immediately fixed on a substrate holder specially designed for glancing angle deposition (Fig. 1(a)) and charged into the vacuum chamber. Six substrate tilt angles θ are available on the substrate-holder: 15, 30, 45, 60, 75, and 90°. The target-to-substrate distance was fixed at 12 cm and the center of each substrate is at 3 cm from the symmetrical axis. A schematic illustration of the geometry of the system is shown in Fig. 1(b).

The substrate tilt angle, θ , is defined as the angle between the normal to the substrate (or substrate-holder) and the normal to the substrate-holder plate, assumed collinear with the normal to the target. The flux incident angle, α , is defined as the angle between the normal to the

substrate and the incidence direction of the impinging flux [34]. The column tilt angle, β , is defined as the angle between the normal to the substrate and the growth direction of the film columns. θ is known thanks to the substrate-holder geometry, α can only be calculated by simulation, and β is determined from the film cross-sections obtained by SEM.

Before deposition, the chamber was pumped down to 2×10^{-4} Pa. The working pressure was fixed to 0.22 Pa with an inlet of 3.5 sccm of pure argon. The discharge voltage was –320 V for an imposed current of 250 mA. The deposition time for each type of substrate (Si, Ti-6Al-4V, and CoCrMo) was 90 min.

The coatings deposited on Si substrates were used to characterize their microstructure and thicknesses, while those on Ti-6Al-4V and CoCrMo substrates were employed to investigate their wear and corrosion behaviors.

2.2. Deposition simulation

The characteristic of the Zr flux was calculated with SiMTRA [35] using the experimental working pressure and system geometry. The initial angular and energy distribution was obtained by SRIM [36] using the experimental ion energy. 10^5 and 10^7 particles were simulated in SRIM and SiMTRA, respectively. Due to the limitations of SEM imagery for accurate thin films density measurements, quantitative pore analyses were performed using the NASCAME porosity plug-in [37] on the digital films obtained with NASCAME (4.6.2) [38]. The substrates had a size of 10×200 particles and the total number of deposited particles ranged between 5×10^5 and 2×10^6 particles based on the SiMTRA outputs. The probe used for the porosity calculation had a size of 3 and 4.

2.3. Characterization and analysis methods

The surface morphology and cross-section of the Zr films with inclined columns were observed by Scanning Electron Microscopy (SEM-JEOL JSM 7610 F). From the cross-section's images, the film thickness, and the column tilt angle β were determined.

In vitro degradation behavior of coated and uncoated alloys was investigated by open circuit potential (OCP) and potentiodynamic polarization. The electrochemical tests were performed in a physiological serum (NaCl 0.9%), considered as the most representative solution of the human body and in an aerated environment at 37 ± 1 °C. Open circuit potential (OCP), or resting potential (E_{rest}), time dependencies were measured, and potentiodynamic polarization tests were performed to study the corrosion behavior of the investigated samples. The potentiodynamic tests were performed using a conventional three-electrode cell with a gold electrode, a saturated calomel reference electrode

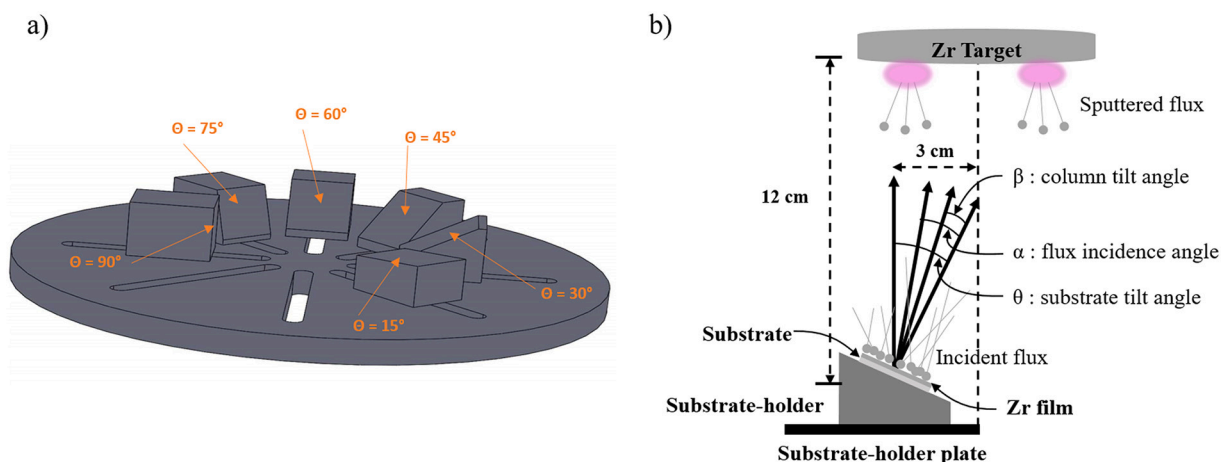


Fig. 1. (a) View of the substrate-holder plate with the six inclined substrate-holders. (b) Schematic illustration of the geometry of the deposition system.

(Hg/Hg₂Cl₂), and the working electrode (coated and uncoated samples). The working electrode areas were respectively 0.62 cm² and 1.13 cm² for CoCrMo and Ti-6Al-4V, corresponding to the top surface of the samples. First, the OCP versus time was monitored without applying any external polarization for 3600 s in 50 mL, until equilibrium was reached at the corrosion potential E_{corr} . Then, a potential was applied, ranging from -1 to +1 V with a scan rate of 1 mV/s, while the corrosion current was measured. For each sample, two specimens were tested in the same conditions. The electrodes were connected to a potentiostat (VOLTALAB PGZ 100) and monitored using the Voltamaster 4 software. From the potentiodynamic curves, using the Tafel extrapolation method, the corrosion current densities i_{corr} (μA/cm²) are obtained and two criteria were calculated: corrosion rate (CR) and protection efficiency (%P.E.). The corrosion rate is determined using Eq. (1) [39]:

$$\text{CR} = 3.27 \cdot 10^{-3} \frac{i_{\text{corr}} E_w}{\rho} \quad (1)$$

where CR is the corrosion rate (mm. year⁻¹), i_{corr} is the corrosion current density (μA.cm⁻²), E_w is the equivalent weight (molar mass divided by the oxidation state) and ρ is the material density (g.cm⁻³).

Table 1 lists the material-dependent values used for the calculation.

The corrosion protection efficiency (%P.E.) is determined using Eq. (2) [40,41]:

$$\%P.E. = 100 \left(1 - \frac{i_{\text{coated}}}{i_{\text{uncoated}}} \right) \quad (2)$$

where i_{coated} is the corrosion current density of the coated sample and i_{uncoated} is the corrosion current density of the uncoated sample.

Several chemical and electrochemical porosity tests are found in the literature. Chemical porosity tests include neutral and acetic acid salt spray, sulfur dioxide exposure, the use of a ferroxy indicator, and corrod-kote corrosion tests [42–44]. These tests are designed to attack the substrate revealing the corrosion occurring through the pores. However, corrosion products could block the pores and give false readings while very small pores are difficult to penetrate by the electrolyte and may be missed. These tests often take a long time and visual results can be difficult to quantify [45]. In contrast, electrochemical tests, such as Tafel extrapolation, cyclic voltammetry, linear polarization resistance, and corrosion potential monitoring, are more quantitative and can be performed rapidly with standard electrochemical instrumentation [46,47].

Based on the Tafel curves, the main electrochemical parameters were extracted and used to calculate the porosity of the coatings using Elsener's equation [48]:

$$P = \left(\frac{R_p, \text{substrate}}{R_p, \text{coating}} \right) \cdot 10^{-\frac{|\Delta E_i=0|}{ba}} \quad (3)$$

where $R_p, \text{substrate}$ is the substrate polarization resistance, $R_p, \text{coating}$ is the coating polarization resistance, $|\Delta E_i=0|$ is the difference between the coatings and the substrate corrosion potentials and ba is the substrate anodic slope.

The polarization resistance (R_p) was calculated using the Stern-Geary equation [49]:

$$R_p = \left(\frac{1}{2.3} \right) \cdot \left(\frac{ba \cdot |bc|}{(ba + |bc|)} \right) \cdot \frac{1}{i_{\text{corr}}} \quad (4)$$

where the i_{corr} is corrosion current density, ba the anodic slope, and bc

Table 1

Estimated parameters for the substrates and the film materials.

	Molar mass (g.mol ⁻¹)	Oxidation state	Density (g.cm ⁻³)
Zr	91.22	4	6.52
Ti-6Al-4V	46.74	4	4.3
CoCrMo	58.67	2–3	8.44

the cathodic slope of the polarization curves.

3. Results and discussion

3.1. Characterization of the Zr flux

Fig. 2 presents the evolution of the flux incidence angle α with the substrate tilt angle θ .

The dashed line represents the absolute equality of the two angles and serves as a reference. As expected from the geometry of the deposition system (dimension of the target, target-to-substrate distance, position of the substrate-holders, working pressure), the flux incidence angle α is not equal to the substrate tilt angle θ . An offset of 14°, increasing to 21° with the substrate tilt angle, is found. The main contribution of this offset is due to the geometry ($\arctan(3/12) \approx 14^\circ$), while the small increase for high substrate tilt angles comes from the increase of the fraction of thermalized atoms compared to the fraction of ballistic atoms. In the following sections, the graphs will be presented function of the flux incidence angle α and not function of the substrate tilt angle θ . The flux incidence angle α is the most relevant parameter to describe the deposition conditions and includes the substrate tilt angle θ . However, the latter can be useful to classify and name the different coatings.

3.2. Thickness and surface morphology of the Zr films

The evolution of the Zr film morphologies (cross-section and top views) with increasing substrate tilt is obtained by SEM and shown in Fig. 3.

The cross-section views presented in Fig. 3 (upper line) show the expected morphologies. The films are columnar, and the increase of the substrate tilt angle is accompanied by an increase of the column tilt angle and a decrease of the film thickness. It can be observed on the top views presented in Fig. 3 (lower line) that the top of the columns for the low substrate tilt angles (15 and 30°) present hexagonal shapes with an average size comprised between 50 and 75 nm. With more tilted substrates (45 and 60°) the shapes of the columns tend to be elongated in the direction perpendicular to the particle flux. The columns size tends to decrease to 30 nm in the direction of the particle flux, while in the direction perpendicular to the particle flux, the size remains in the same dimension as previously observed for low substrate tilt angles. With the highest substrate tilts the columns are smaller (about 30 nm) and intercolumnar voids are observed. This is obviously linked to higher film roughness and porosity, which will influence the corrosion resistance. These morphologies are fully consistent with the numerous studies on

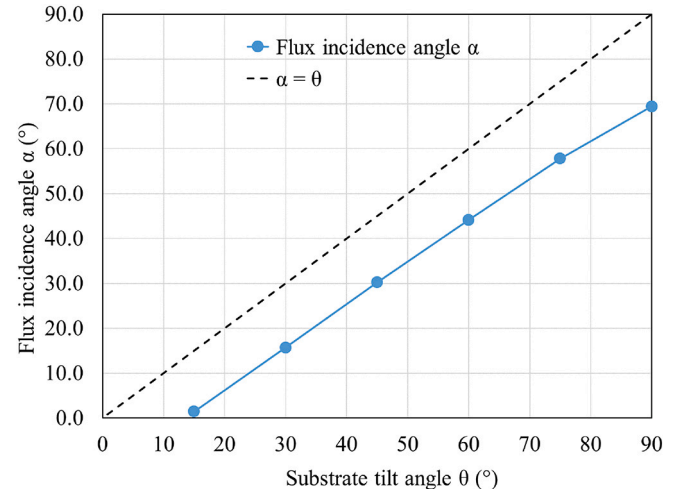


Fig. 2. Evolution of the flux incidence angle α with the substrate tilt angle θ .

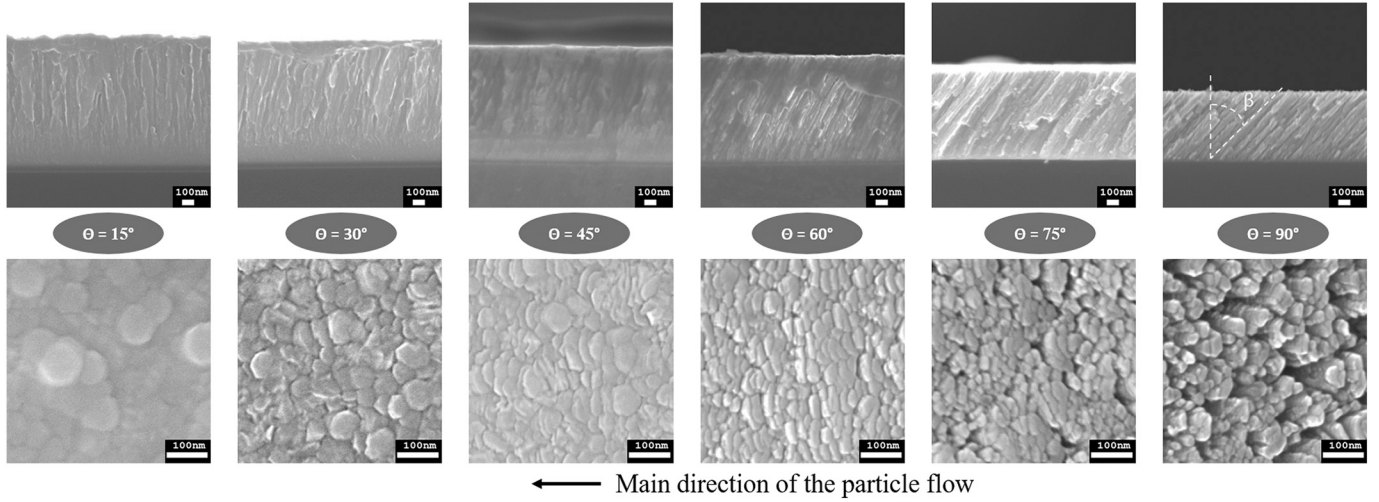


Fig. 3. SEM cross-section (upper line) and surface top views (lower line) of Zr films deposited at substrate tilt angle θ of 15, 30, 45, 60, 75, and 90° on silicon.

OAD for other material systems [50–53].

From the SEM cross-sections (Fig. 3, upper line), the film thickness t and the column tilt angle (β) can be readily measured. The evolution of these two parameters with the flux incidence angle α is presented in Fig. 4.

The average film thickness was measured by SEM in three zones (top, middle, and bottom of the substrate) to take into account any variation. As observed on the SEM images, the thickness of the Zr films exhibits a decreasing trend with the increase of the flux incidence angle α (Fig. 4 (a)). The cosine of the incidence angle α is presented as a reference. Indeed, the theoretical OAD film thickness is expected to be proportional to the projected substrate surface in a plane parallel to the target. The film thickness varies from 1000 to 500 nm with a cosine-like evolution. However, the data are slightly higher than the expected cosine reference. This can be explained by two points: there are some dispersions in the particle flux and the source is not punctual. The first point is due to the working pressure and implies that the impinging atoms do not have parallel directions. Consequently, atoms coming from the whole space can reach the substrate. The second point is due to the size of the racetrack of the target, i.e. the geometrical substrate tilt angle will vary by $\pm 5^\circ$. Combining these two effects, it is obvious that the number of atoms impinging on the substrates, and consequently the film thickness, will be higher than the one predicted by the cosine evolution.

The evolution of the experimental column tilt angle is presented in Fig. 4(b) with the two most frequent theoretical rules: Tait's rule and the tangent rule (Eqs. (5) and (6), respectively)

$$\beta = \alpha - \arcsin\left(\frac{1 - \cos(\theta)}{2}\right), \quad (5)$$

$$\tan\beta = \frac{\tan\alpha}{2} \quad (6)$$

The column tilt angle increases with the incidence flux angle from 3 to 42° with a “Tait's rule”-like evolution. For incidence angles higher than 15°, the column tilt values are lower than the ones predicted by Tait's rule. Once again, this is due to the scattering during transport and the geometrical configuration (position of the substrate and size of the racetrack), i.e. the fraction of the flux with a low incidence angle is increasing with the substrate tilt angle.

3.3. Resting potential

The influence of the surface treatment on the polarization behavior in a 0.9% NaCl solution of the CoCrMo and Ti-6Al-4V alloys was first studied. Open circuit potential (OCP) is an important tool to investigate the corrosion behavior of the studied electrodes. It indicates the tendency of the tested electrode to electrochemical dissolution/passivation in a test solution [54].

Fig. 5(a) presents the evolution of the steady-state open circuit potential (E) for uncoated and Zr-coated CoCrMo and Ti-6Al-4V tested samples as a function of the flux incidence angle.

Uncoated Ti-6Al-4V and CoCrMo present a resting potential of -184

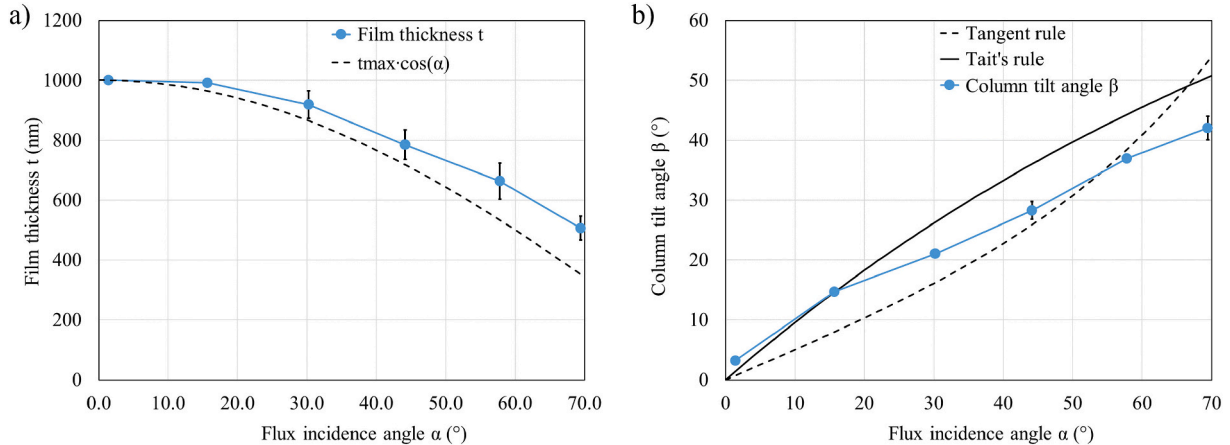


Fig. 4. (a) Film thickness and (b) column tilt angle β as a function of the flux incidence angle α .

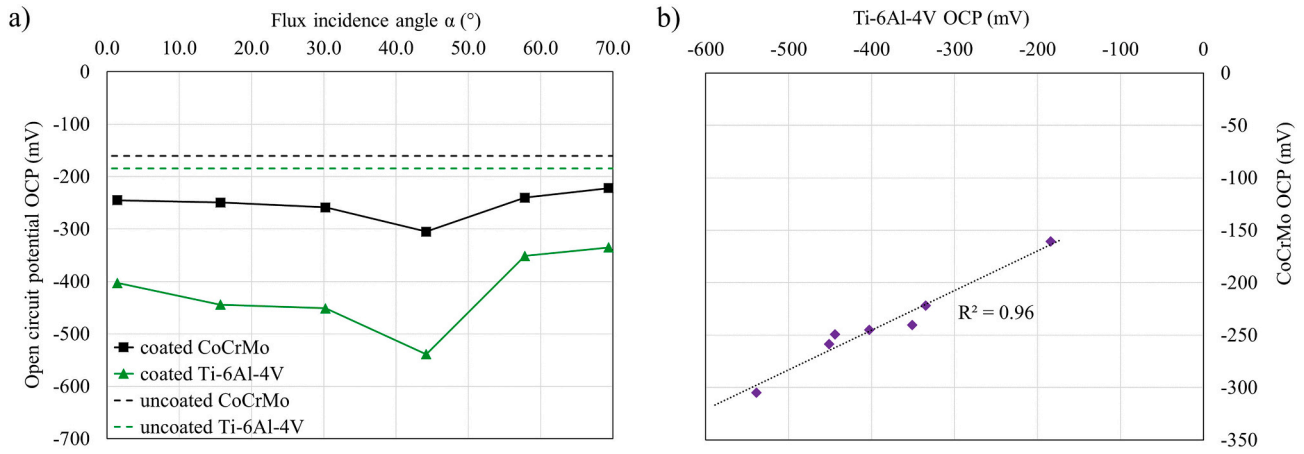


Fig. 5. (a) Open circuit potential of uncoated and Zr-coated CoCrMo and Ti-6Al-4V obtained versus the flux incidence angle α . (b) Ti-6Al-4V open circuit potential versus CoCrMo open circuit potential.

and -160 mV, respectively; CoCrMo tends to be nobler than Ti-6Al-4V. All Zr-coated samples present a higher negative resting potential, proof that the substrates remain fully protected after the deposition of the coating. The coated CoCrMo samples have always a nobler behavior than the coated Ti-6Al-4V ones, indicating that the couple substrate-coating has to be considered as a whole. However, the resting potential of the coated samples shows variations, which can be grouped in two zones. The first zone for flux incidence angles α smaller than 45° and the second for flux incidence angles α higher than 45° . In the first zone, the resting potential continuously decreases from -402 to -538 mV and from -245 to -304 mV for coated Ti-6Al-4V and CoCrMo, respectively. The decrease is more marked for the transition between 30 and 44.2° . Then, the resting potential increases suddenly to the second zone, where a slight increase from -351 to -334 mV and from -240 to -222 mV is observed for coated Ti-6Al-4V and CoCrMo, respectively. These variations are related to the film's properties varying with the flux incidence angle (column shapes, roughness, porosity, etc.). Fig. 5(b) presents the OCP for the uncoated and Zr-coated Ti-6Al-4V compared to the OCP for the uncoated and Zr-coated CoCrMo. A linear relation is found between both behaviors, indicating that the properties of the films are responsible for these variations. Indeed, the only variable in this set of data is the deposition conditions that drive the film's microstructures and consequently their properties, i.e. thickness and porosity. Some effects of coatings porosity, leading to a marked decrease in corrosion resistance with lower layer densities have already been shown in the literature [47]. The decrease in open circuit potential with flux incidence angle at

angles lower than 45° finds its origin in a small increase of the porosity combined with the decrease of the film thickness (Fig. 4(a)), while the sudden increase of the potential for higher incidence angles can be attributed to the appearance of intercolumnar voids, as observed on Fig. 3. The validity of this hypothesis has been evaluated through the NASCAM simulations and calculation of Zr coatings porosity, detailed in Section 3.5.

3.4. Potentiodynamic polarization curves

Resting potential tests are insufficient for the determination of the corrosion resistance, especially regarding the short immersion time of 1 h used in the experiments. Polarization curves are more appropriate to study the full range of corrosion resistance. From the polarization curves (see Fig. S1 and Table S2 in Supplementary data) the corrosion current density i_{corr} is determined and the corrosion rate and protection efficiency are calculated. Fig. 6(a) presents the corrosion rate for the uncoated and Zr-coated CoCrMo and Ti-6Al-4V samples.

Even if the CoCrMo tends to be nobler than Ti-6Al-4V, the corrosion rate is about three times higher, i.e. 281 and 84 $\mu\text{m}/\text{yr}$, respectively. This can be explained by the higher passivation ability of the Ti-6Al-4V, leading to the formation of a protective oxide layer at the surface of the sample [55–57]. Zirconium, as a transition metal, presents also a passivation behavior [58,59] and protects the substrates thanks to a lower OCP. Thus, as seen in Fig. 6, the coated samples always present a lower corrosion rate than the uncoated alloys, i.e. the coated samples

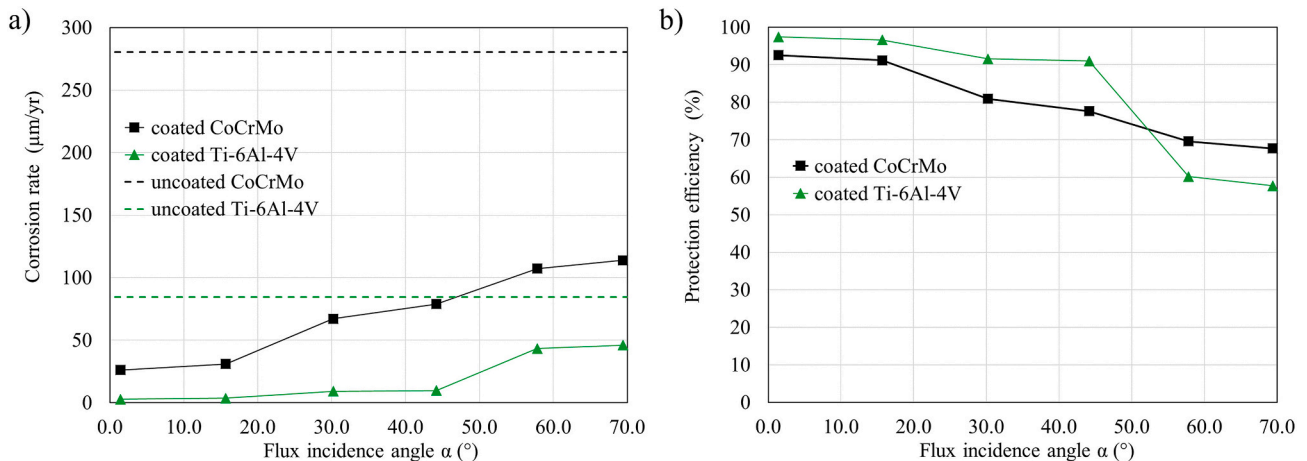


Fig. 6. (a) Corrosion rate and (b) protection efficiency versus with the flux incidence angle α for uncoated and Zr-coated CoCrMo and Ti-6Al-4V alloys.

exhibited a good corrosion resistance and permitted an excellent protection efficiency.

However, the influence of the film microstructure is obvious, i.e. with the increase of the flux incidence angle the corrosion rate increases. The influence of the corrosion rate can be quantified thanks to the protection efficiency presented in Fig. 6(b). In the case of the Ti-6Al-4V substrate, the Zr coating offers a protection efficiency between 97 and 91% for incidence angles smaller than 45° . Above this angle, the protection decreases to 60%. The same behavior is observed for the CoCrMo substrate, except that the variations are less important. The protection begins with a level of 93% and progressively decreases to 77.6% for the incidence angle of 44.2° . Then a drop of about 10% occurs for higher incidence angles.

This protection efficiency decrease, i.e. the corrosion current density increase, may be due to the increase of the film porosity with the flux incidence angle. The incidence angle allows the solution to reach the substrate and exchange ions. The protection remains relatively high due to a partial clogging of the pore with the corrosion products. These products hinder the anodic dissolution, protecting the substrate [60,61].

The difference between the Zr-coated CoCrMo and the Zr-coated Ti-6Al-4V can be explained by the open circuit corrosion potential. Among the three materials, CoCrMo is the nobler one and zirconium the less noble. The corrosion of the Zr coating will then be sped up by the difference of potential, leading to this progressive protection efficiency decrease. For coated Ti-6Al-4V, this difference of potential is smaller, giving time to the film to close the porosity and to protect the substrate, except when the porosity passes a threshold value.

3.5. Film porosity

The porosity of the Zr coatings on CoCrMo and Ti-6Al-4V alloys was examined using the Tafel extrapolations. Fig. 7(a) presents the calculated experimental porosity versus the flux incidence angle α .

Both coated samples present the same behavior. A low and stable porosity at low incidence angles ($\alpha < 45^\circ$) followed by a sudden increase at higher incidence angles ($\alpha > 45^\circ$). In the first zone, the film porosity is about 0.2 and 2.3% for Ti-6Al-4V and CoCrMo, respectively. In the second zone, the increase is about 4.5 and 6% per 10° for Ti-6Al-4V and CoCrMo, respectively. The offset of 2–3% found between the Ti-6Al-4V and CoCrMo series is due to the influence of the substrates, i.e. the CoCrMo samples have higher potentials and corrosion current densities than the Ti-6Al-4V ones. These electrical differences will affect the porosity calculation by increasing the values.

In order to confirm that the corrosion behavior finds its origin in the film porosity, which is directly due to the inclined columnar film microstructure, simulations of the film's porosity were performed with

NASCAM. Fig. 7(b) presents the experimental porosity of Zr coatings versus the simulated one. An excellent correlation is found between the experimental and simulated results with an R^2 of 0.96, definitely confirming the role of the film porosity on the corrosion resistance performance. Moreover, it proves that the deposition process, which can be fully reproduced by simulation, is directly responsible for the microstructural changes and the subsequent film properties.

4. Conclusion

Detailed analysis of the corrosion behavior of PVD Zr-coated Ti-6Al-4V and CoCrMo alloys with different substrates angles through electrochemical studies in 37°C NaCl (0.9%)'s solution allowed to determine the effect of Zr coatings deposited on a hemispherical prosthesis. Summarizing the research conducted in this article, it can be stated that:

- A substrate-holder composed of six different substrates tilt angles (15 to 90° with 15° increments) allowed to model the deposition on several locations on a hemispherical prosthesis.
- The film's microstructures present the expected evolutions with the flux incidence angle: cosine decrease of the thickness (from 1000 to 500 nm), increase of the column tilt angle following the Tait's rule (from 3 to 42°), and changes in the top surface morphologies.
- All coated samples (Ti-6Al-4V and CoCrMo) present better resistance to electrochemical corrosion in comparison to the uncoated substrates, with an increase of the negative potential by a factor 2 on average.
- The corrosion rate tends to increase with the flux incidence angle, corresponding to a decrease of the protection efficiency from about 95% to 65% on average.
- The corrosion behavior of the coated substrates revealed several points or critical zones in comparison to the substrate inclination angle. The flux incidence angle of 45° seems to be the pivotal angle. For flux angles lower than 45° the films are dense (less than 5% of porosity) and provide good corrosion protection, however, for flux angles higher than 45° the film's porosity increases (up to 12–18%) and deteriorates the corrosion protection.
- The Zr columnar thin films are a promising approach for biomedical uses, including implant applications, due to their improved surface corrosion protection in physiological media if the microstructure is finely controlled especially thanks to the use of the simulation.

CRedit authorship contribution statement

Khaoula Rahmouni: Writing – original draft, Writing – review & editing, Visualization, Resources, Conceptualization, Software.

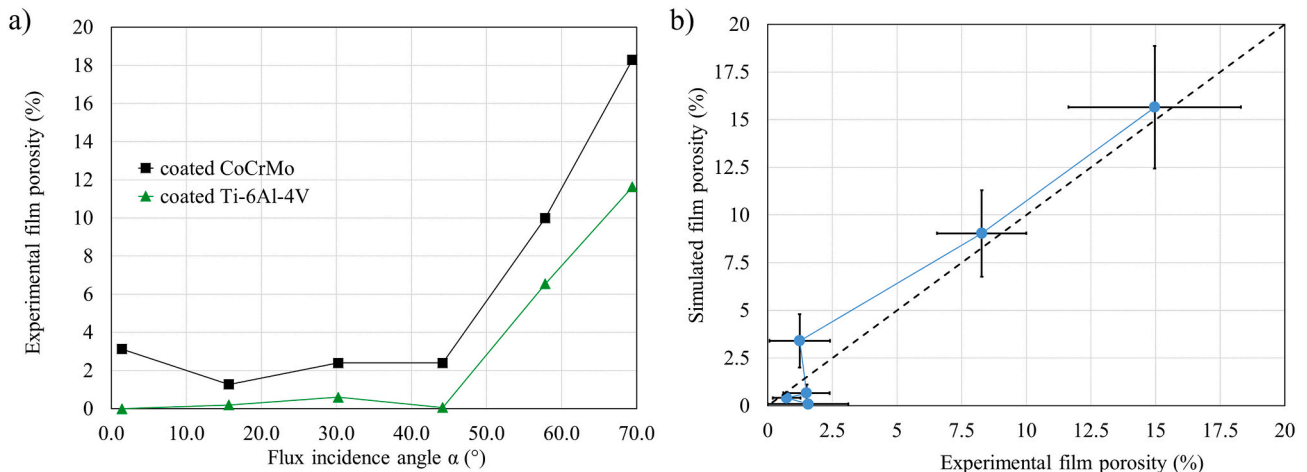


Fig. 7. (a) Experimental film porosity versus the flux incidence angle α . (b) Experimental film porosity of Zr coatings versus the simulated film porosity.

Aurélien Besnard: Supervision, Data curation, Writing – original draft, Conceptualization, Methodology, Visualization, Software. **Kafia Oulmi:** Data curation, Conceptualization, Methodology, Software, Writing – review & editing. **Corinne Nouveau:** Resources, Writing – review & editing. **Aissam Hidoussi:** Software, Formal analysis. **Linda Aissani:** Funding acquisition. **Mourad Zaabat:** Project administration, Funding acquisition.

Declaration of competing interest

The authors declare that they have no known competing financial interests or personal relationships that could have appeared to influence the work reported in this paper.

Acknowledgments

This research work receives funding from the PROFAS B+ doctoral scholarships.

Appendix A. Supplementary data

Supplementary data to this article can be found online at <https://doi.org/10.1016/j.surfcoat.2022.128310>.

References

- [1] G. Pezzotti, K. Yamamoto, Artificial hip joints: the biomaterials challenge, *J. Mech. Behav. Biomed. Mater.* 31 (2014) 3–20, <https://doi.org/10.1016/j.jmbbm.2013.06.001>.
- [2] G. Shen, J.-F. Zhang, F.-Z. Fang, In vitro evaluation of artificial joints: a comprehensive review, *Adv. Manuf.* 7 (2019) 1–14, <https://doi.org/10.1007/s40436-018-00244-z>.
- [3] D. Choudhury, J.M. Lackner, L. Major, T. Morita, Y. Sawae, A. Bin Mamat, I. Stavness, C.K. Roy, I. Krupka, Improved wear resistance of functional diamond like carbon coated Ti–6Al–4V alloys in an edge loading conditions, *J. Mech. Behav. Biomed. Mater.* 59 (2016) 586–595, <https://doi.org/10.1016/j.jmbbm.2016.04.004>.
- [4] S. Kurtz, K. Ong, E. Lau, F. Mowat, M. Halpern, Projections of primary and revision hip and knee arthroplasty in the United States from 2005 to 2030, *JBJS* 89 (2007) 780–785, <https://doi.org/10.2106/JBJS.F.00222>.
- [5] L.E. Bayliss, D. Culliford, A.P. Monk, S. Glyn-Jones, D. Prieto-Alhambra, A. Judge, C. Cooper, A.J. Carr, N.K. Arden, D.J. Beard, A.J. Price, The effect of patient age at intervention on risk of implant revision after total replacement of the hip or knee: a population-based cohort study, *Lancet* 389 (2017) 1424–1430, [https://doi.org/10.1016/S0140-6736\(17\)30059-4](https://doi.org/10.1016/S0140-6736(17)30059-4).
- [6] J. Gallo, E. Gibon, S.B. Goodman, Chapter 4 - implants for joint replacement of the hip and knee, in: S. Bose, A. Bandyopadhyay (Eds.), *Mater. Bone Disord*, Academic Press, 2017, pp. 119–196, <https://doi.org/10.1016/B978-0-12-802792-9.00004-5>.
- [7] S.B. Goodman, E. Gómez Barrena, M. Takagi, Y.T. Kontinen, Biocompatibility of total joint replacements: a review, *J. Biomed. Mater. Res. A* 90A (2009) 603–618, <https://doi.org/10.1002/jbm.a.32063>.
- [8] C.B. Rieker, R. Schön, P. Köttig, Development and validation of a second-generation metal-on-metal bearing: laboratory studies and analysis of retrievals, *J. Arthroplast.* 19 (2004) 5–11, <https://doi.org/10.1016/j.arth.2004.09.017>.
- [9] J.P.L. do Nascimento, M.O.A. Ferreira, R.V. Gelamo, J. Scarminio, T.T. Steffen, B. P. da Silva, I.V. Aoki, A.G. dos Santos Jr., V.V. de Castro Jr., C. de Fraga Malfatti Jr., J.A. Moreto Jr., Enhancing the corrosion protection of Ti–6Al–4V alloy through reactive sputtering niobium oxide thin films, *Surf. Coat. Technol.* 428 (2021), 127854, <https://doi.org/10.1016/j.surfcoat.2021.127854>.
- [10] J.T. Philip, J. Mathew, B. Kuriachen, Tribology of Ti6Al4V: a review, *Friction* 7 (2019) 497–536, <https://doi.org/10.1007/s40544-019-0338-7>.
- [11] F. Gao, W. Li, B. Meng, M. Wan, X. Zhang, X. Han, Rheological law and constitutive model for superplastic deformation of ti-6Al-4V, *J. Alloys Compd.* 701 (2017) 177–185, <https://doi.org/10.1016/j.jallcom.2017.01.096>.
- [12] J.N. Oliver, Y. Su, X. Lu, P.-H. Kuo, J. Du, D. Zhu, Bioactive glass coatings on metallic implants for biomedical applications, *Bioact. Mater.* 4 (2019) 261–270, <https://doi.org/10.1016/j.bioactmat.2019.09.002>.
- [13] K. Aniolek, M. Kupka, Surface characterization of thermally oxidized ti-6Al-7Nb alloy, *Mater. Chem. Phys.* 171 (2016) 374–378, <https://doi.org/10.1016/j.matchemphys.2016.01.031>.
- [14] S. Zhang, J. Qin, C. Yang, X. Zhang, R. Liu, Effect of zr addition on the microstructure and tribological property of the anodization of ti-6Al-4V alloy, *Surf. Coat. Technol.* 356 (2018) 38–48, <https://doi.org/10.1016/j.surfcoat.2018.09.051>.
- [15] C.A.R. Maestro, J.A. Moreto, T. Chiamonte, R.V. Gelamo, C.J.F. de Oliveira, M. M. Santos, M.V. da Silva, A.H.S. Bueno, R.M. Balestra, A.M. de Sousa Malafaia, Corrosion behavior and biological responses of a double coating formed on the ti-6Al-4V alloy surface by using thermal oxidation and biomimetic deposition of bismuth-doped CaP, *Surf. Coat. Technol.* 425 (2021), 127717, <https://doi.org/10.1016/j.surfcoat.2021.127717>.
- [16] W.Q. Bai, L.L. Li, R.L. Li, C.D. Gu, X.L. Wang, G. Jin, D.G. Liu, J.P. Tu, Deposition and characterization of a Zn/Ni/a-C multilayer: implication on bio-tribological and corrosion behaviors, *Surf. Coat. Technol.* 324 (2017) 509–517, <https://doi.org/10.1016/j.surfcoat.2017.05.058>.
- [17] G. Rosas-Becerra, I. Mejía-Caballero, J. Martínez-Trinidad, M. Palomar-Pardavé, M. Romero-Romo, R. Pérez-Pasten-Borja, I. Campos-Silva, Electrochemical corrosion behavior of borided CoCrMo alloy immersed in hanks' solution, *J. Mater. Eng. Perform.* 26 (2017) 704–714, <https://doi.org/10.1007/s11665-017-2513-1>.
- [18] M.A. Doñu-Ruiz, N. López-Perrusquia, A. Renteria-Salcedo, M. Flores-Martinez, E. Rodríguez-De Anda, S. Muhl, C. Hernández-Navarro, E. García, Tribocorrosion behavior of boride coating on CoCrMo alloy produced by thermochemical process in 0.35% NaCl solution, *Surf. Coat. Technol.* 425 (2021), 127698, <https://doi.org/10.1016/j.surfcoat.2021.127698>.
- [19] A. Olajinka, A. Esther, O. Philip, Examination of electrochemical corrosion properties of titanium carbide thin film grown by RF magnetron sputtering, *Mater. Today Proc.* 44 (2021) 994–999, <https://doi.org/10.1016/j.matpr.2020.11.170>.
- [20] A.M. Oje, A.A. Ogwu, A.I. Oje, N. Tsendzughul, S. Ur Rahman, A comparative study of the corrosion and ion release behaviour of chromium oxide coatings exposed to saline, Ringer's and Hank's physiological solutions, *Corros. Sci.* 167 (2020), 108533, <https://doi.org/10.1016/j.corsci.2020.108533>.
- [21] C.A.R. Maestro, J.A. Moreto, T. Chiamonte, R.V. Gelamo, C.J.F. de Oliveira, M. M. Santos, M.V. da Silva, A.H.S. Bueno, R.M. Balestra, A.M. de Sousa Malafaia, Corrosion behavior and biological responses of a double coating formed on the ti-6Al-4V alloy surface by using thermal oxidation and biomimetic deposition of bismuth-doped CaP, *Surf. Coat. Technol.* 425 (2021), 127717, <https://doi.org/10.1016/j.surfcoat.2021.127717>.
- [22] C.-E. Tsai, J. Hung, Y. Hu, D.-Y. Wang, R.M. Pilliar, R. Wang, Improving fretting corrosion resistance of CoCrMo alloy with TiSiN and Zn coatings for orthopedic applications, *J. Mech. Behav. Biomed. Mater.* 114 (2021), 104233, <https://doi.org/10.1016/j.jmbbm.2020.104233>.
- [23] S. Datta, M. Das, V.K. Balla, S. Bodhak, V.K. Murugesan, Mechanical, wear, corrosion and biological properties of arc deposited titanium nitride coatings, *Surf. Coat. Technol.* 344 (2018) 214–222, <https://doi.org/10.1016/j.surfcoat.2018.03.019>.
- [24] J.E. Gray, B. Luan, Protective coatings on magnesium and its alloys — a critical review, *J. Alloys Compd.* 336 (2002) 88–113, [https://doi.org/10.1016/S0925-8388\(01\)01899-0](https://doi.org/10.1016/S0925-8388(01)01899-0).
- [25] Y. Xin, C. Liu, K. Huo, G. Tang, X. Tian, P.K. Chu, Corrosion behavior of Zn/Ni coated biomedical AZ91 magnesium alloy, *Surf. Coat. Technol.* 203 (2009) 2554–2557, <https://doi.org/10.1016/j.surfcoat.2009.02.074>.
- [26] R. Hübler, A. Cozza, T.L. Marcondes, R.B. Souza, F.F. Fiori, Wear and corrosion protection of 316-L femoral implants by deposition of thin films, *Surf. Coat. Technol.* 142–144 (2001) 1078–1083, [https://doi.org/10.1016/S0257-8972\(01\)01321-4](https://doi.org/10.1016/S0257-8972(01)01321-4).
- [27] W.-J. Chou, G.-P. Yu, J.-H. Huang, Corrosion resistance of Zn films on AISI 304 stainless steel substrate, *Surf. Coat. Technol.* 167 (2003) 59–67, [https://doi.org/10.1016/S0257-8972\(02\)00882-4](https://doi.org/10.1016/S0257-8972(02)00882-4).
- [28] Y. Cheng, Y.F. Zheng, A study of Zn/Ni coatings deposited on NiTi alloy by PIIIID technique, *IEEE Trans. Plasma Sci.* 34 (2006) 1105–1108, <https://doi.org/10.1109/TPS.2006.877502>.
- [29] J. Han, F. Zhang, B. Van Meerbeek, J. Vleugels, A. Braem, S. Castagne, Laser surface texturing of zirconia-based ceramics for dental applications: a review, *Mater. Sci. Eng. C* 123 (2021), 112034, <https://doi.org/10.1016/j.msec.2021.112034>.
- [30] R. Patil, Zirconia versus titanium dental implants: a systematic review, *J. Dent. Implants* 5 (2015) 39, <https://doi.org/10.4103/0974-6781.154430>.
- [31] A. Brizuela-Velasco, E. Pérez-Pevida, A. Jiménez-Garrudo, F.J. Gil-Mur, J. M. Manero, M. Punset-Fuste, D. Chávarri-Prado, M. Diéguez-Pereira, F. Monticelli, Mechanical characterisation and biomechanical and biological behaviours of ti-zr binary-alloy dental implants, *Biomed. Res. Int.* 2017 (2017), e2785863, <https://doi.org/10.1155/2017/2785863>.
- [32] N. Saulacic, D. Bosshardt, M. Bornstein, S. Berner, D. Buser, Bone apposition to a titanium-zirconium alloy implant, as compared to two other titanium-containing implants, *Eur. Cell. Mater.* 23 (2012) 273–286.
- [33] H.M. Grandin, S. Berner, M. Dard, A review of titanium zirconium (TiZr) alloys for use in endosseous dental implants, *Materials* 5 (2012) 1348–1360, <https://doi.org/10.3390/ma5081348>.
- [34] A. Siad, A. Besnard, C. Nouveau, P. Jacquet, Critical angles in DC magnetron glad thin films, *Vacuum* 131 (2016) 305–311, <https://doi.org/10.1016/j.vacuum.2016.07.012>.
- [35] K.V. Aeken, S. Mahieu, D. Depla, The metal flux from a rotating cylindrical magnetron: a Monte Carlo simulation, *J. Phys. Appl. Phys.* 41 (2008), 205307, <https://doi.org/10.1088/0022-3727/41/20/205307>.
- [36] J.F. Ziegler, J.P. Biersack, The stopping and range of ions in matter, in: D. A. Bromley (Ed.), *Treatise Heavy-Ion Sci. Vol. 6 Astrophys. Chem. Condens. Matter*, Springer US, Boston, MA, 1985, pp. 93–129, https://doi.org/10.1007/978-1-4615-8103-1_3.
- [37] V. Godinho, P. Moskovkin, R. Álvarez, J. Caballero-Hernández, R. Schierholz, B. Bera, J. Demarche, A. Palmero, A. Fernández, S. Lucas, On the formation of the porous structure in nanostructured a-si coatings deposited by dc magnetron sputtering at oblique angles, *Nanotechnology* 25 (2014), 355705, <https://doi.org/10.1088/0957-4484/25/35/355705>.
- [38] J. Dervaux, P.-A. Cormier, P. Moskovkin, O. Douheret, S. Konstantinidis, R. Lazzaroni, S. Lucas, R. Snyders, Synthesis of nanostructured ti thin films by

combining glancing angle deposition and magnetron sputtering: a joint experimental and modeling study, *Thin Solid Films* 636 (2017) 644–657, <https://doi.org/10.1016/j.tsf.2017.06.006>.

- [39] R.J. Guillory, M. Sikora-Jasinska, J.W. Drelich, J. Goldman, In vitro corrosion and in vivo response to zinc implants with electropolished and anodized surfaces, *ACS Appl. Mater. Interfaces* 11 (2019) 19884–19893, <https://doi.org/10.1021/acsmi.9b05370>.
- [40] K. Nozawa, K. Aramaki, One- and two-dimensional polymer films of modified alkanethiol monolayers for preventing iron from corrosion, *Corros. Sci.* 41 (1999) 57–73, [https://doi.org/10.1016/S0010-938X\(98\)00048-1](https://doi.org/10.1016/S0010-938X(98)00048-1).
- [41] A. Vladescu, V. Pruna, S. Kulesza, V. Braic, I. Titorencu, M. Bramowicz, A. Gozdziewska, A. Parau, C.M. Cotrut, I. Pana, M. Dinu, M. Braic, Influence of Ti, Zr or Nb carbide adhesion layers on the adhesion, corrosion resistance and cell proliferation of titania doped hydroxyapatite to the Ti6Al4V alloy substrate, utilizable for orthopaedic implants, *Ceram. Int.* 45 (2019) 1710–1723, <https://doi.org/10.1016/j.ceramint.2018.10.053>.
- [42] P. Ernst, I.P. Wadsworth, G.W. Marshall, Porosity of electroless nickel coatings investigated using different porosity tests and their application, *Trans. IMF* 75 (1997) 194–198, <https://doi.org/10.1080/00202967.1997.11871171>.
- [43] P. Leisner, M.E. Benzon, Porosity measurements on coatings, *Trans. IMF* 75 (1997) 88–92, <https://doi.org/10.1080/00202967.1997.11871149>.
- [44] F.C. Walsh, C. Ponce de León, C. Kerr, S. Court, B.D. Barker, Electrochemical characterisation of the porosity and corrosion resistance of electrochemically deposited metal coatings, *Surf. Coat. Technol.* 202 (2008) 5092–5102, <https://doi.org/10.1016/j.surfcoat.2008.05.008>.
- [45] C. Kerr, D. Barker, F. Walsh, Electrochemical techniques for the evaluation of porosity and corrosion rate for electroless nickel deposits on steel, *OnePetro*, 1997 (accessed November 29, 2021), <https://onepetro.org/NACECORR/proceedings/CORR97/ALL-CORR97/NACE-97269/113379>.
- [46] J. Creus, H. Mazille, H. Idrissi, Porosity evaluation of protective coatings onto steel, through electrochemical techniques, *Surf. Coat. Technol.* 130 (2000) 224–232, [https://doi.org/10.1016/S0257-8972\(99\)00659-3](https://doi.org/10.1016/S0257-8972(99)00659-3).
- [47] F. Sittner, W. Ensinger, Electrochemical investigation and characterization of thin-film porosity, *Thin Solid Films* 515 (2007) 4559–4564, <https://doi.org/10.1016/j.tsf.2006.11.031>.
- [48] B. Elsener, A. Rota, H. Böhm, Impedance study on the corrosion of PVD and CVD titanium nitride coatings, *Mater. Sci. Forum* 44–45 (1989) 29–38, <https://doi.org/10.4028/www.scientific.net/MSF.44-45.29>.
- [49] M. Stern, A.L. Geary, Electrochemical polarization: I. A theoretical analysis of the shape of polarization curves, *J. Electrochem. Soc.* 104 (1957) 56, <https://doi.org/10.1149/1.2428496>.
- [50] S. Mahieu, P. Ghekiere, D. Depla, R. De Gryse, Biaxial alignment in sputter deposited thin films, *Thin Solid Films* 515 (2006) 1229–1249, <https://doi.org/10.1016/j.tsf.2006.06.027>.
- [51] A. Barranco, A. Borras, A.R. Gonzalez-Elipe, A. Palmero, Perspectives on oblique angle deposition of thin films: from fundamentals to devices, *Prog. Mater. Sci.* 76 (2016) 59–153, <https://doi.org/10.1016/j.pmatsci.2015.06.003>.
- [52] L.A. Zepeda-Ruiz, G.H. Gilmer, C.C. Walton, A.V. Hamza, E. Chason, Surface morphology evolution during sputter deposition of thin films – lattice Monte Carlo simulations, *J. Cryst. Growth* 312 (2010) 1183–1187, <https://doi.org/10.1016/j.jcrysgro.2009.12.035>.
- [53] G. Abadías, W.P. Leroy, S. Mahieu, D. Depla, Influence of particle and energy flux on stress and texture development in magnetron sputtered TiN films, *J. Phys. Appl. Phys.* 46 (2012), 055301, <https://doi.org/10.1088/0022-3727/46/5/055301>.
- [54] A.M. Fekry, Electrochemical behavior of a novel nano-composite coat on Ti alloy in phosphate buffer solution for biomedical applications, *RSC Adv.* 6 (2016) 20276–20285, <https://doi.org/10.1039/C6RA01064D>.
- [55] J. Yang, H. Yang, H. Yu, Z. Wang, X. Zeng, Corrosion behavior of additive manufactured Ti-6Al-4V alloy in NaCl solution, *Metall. Mater. Trans. A* 48 (2017) 3583–3593, <https://doi.org/10.1007/s11661-017-4087-9>.
- [56] X. Fang, S. Wang, D. Li, Y. Guo, N. Hu, Effect of synovial fluid temperature on the corrosion resistance of Ti6Al4V, Ti6Al7Nb, and CoCrMo alloys, *Mater. Corros.* 71 (2020) 1346–1360, <https://doi.org/10.1002/maco.202011530>.
- [57] Z. Guo, X. Pang, Y. Yan, K. Gao, A.A. Volinsky, T.-Y. Zhang, CoCrMo alloy for orthopedic implant application enhanced corrosion and tribocorrosion properties by nitrogen ion implantation, *Appl. Surf. Sci.* 347 (2015) 23–34, <https://doi.org/10.1016/j.apsusc.2015.04.054>.
- [58] F. Ionescu, L. Reclaru, L.C. Ardelean, A. Blatter, Comparative analysis of the corrosion resistance of titanium alloys intended to come into direct or prolonged contact with live tissues, *Materials* 12 (2019) 2841, <https://doi.org/10.3390/ma12172841>.
- [59] C. Liu, P.K. Chu, G. Lin, D. Yang, Effects of Ti/TiN multilayer on corrosion resistance of nickel–titanium orthodontic brackets in artificial saliva, *Corros. Sci.* 49 (2007) 3783–3796, <https://doi.org/10.1016/j.corsci.2007.03.041>.
- [60] G. Jin, C. Xu, S. Hu, X. Zhou, Temperature dependent electrochemical equilibrium diagram of zirconium–water system studied with density functional theory and experimental thermodynamic data, *J. Nucl. Mater.* 532 (2020), 152036, <https://doi.org/10.1016/j.jnucmat.2020.152036>.
- [61] J. Vega, H. Scheerer, G. Andersohn, M. Oechsner, Experimental studies of the effect of Ti interlayers on the corrosion resistance of TiN PVD coatings by using electrochemical methods, *Corros. Sci.* 133 (2018) 240–250, <https://doi.org/10.1016/j.corsci.2018.01.010>.